New Journal of Physics
The open-access journal for physics

Erratum

Spatially resolved three-dimensional particle dynamics in the void of dusty plasmas under microgravity using stereoscopy

Birger Buttenschön, Michael Himpel and André Melzer 2011 *New J. Phys.* **13** 023042

New Journal of Physics **13** (2011) 059601
Received 9 March 2011
Published 10 May 2011
Online at http://www.njp.org/
doi:10.1088/1367-2630/13/5/059601

The caption of figure 5 was erroneous and should have read as follows:

Trajectory of a selected particle with a length of 40 frames. The graphs show the x-, y- and z-components of (a) the particle position, (b) the particle velocity and (c) the acceleration. (a) Symbols are the raw data, lines the Savitzky–Golay filtered data; (b) symbols are the derivative of the filtered position data, lines are the Savitzky–Golay filtered derivatives; (c) symbols are the derivative of the filtered velocity data, lines are the Savitzky–Golay filtered derivatives.

New Journal of Physics
The open-access journal for physics

Spatially resolved three-dimensional particle dynamics in the void of dusty plasmas under microgravity using stereoscopy

Birger Buttenschön[1], **Michael Himpel and André Melzer**
Institut für Physik, Ernst-Moritz-Arndt-Universität Greifswald,
17487 Greifswald, Germany
E-mail: buttenschoen@physik.uni-greifswald.de

New Journal of Physics **13** (2011) 023042 (19pp)
Received 12 November 2010
Published 28 February 2011
Online at http://www.njp.org/
doi:10.1088/1367-2630/13/2/023042

Abstract. Three-dimensional (3D) dynamical properties of fast particles being injected into the void region of a dusty plasma under microgravity conditions have been measured. For that purpose, a stereoscopic camera setup of three cameras has been developed that is able to track and reconstruct the 3D trajectories of individual dust particles. From more than 500 particle trajectories, the force field inside the void region and its influence on particle movement are derived and analyzed in 3D. It is shown that the force field is dominated by forces pointing radially out of the void and that this radial character is reflected in the velocity distributions of particles leaving the void. Furthermore, the structure of the force field is used for measuring the neutral gas friction for the particles inside the void.

[1] Author to whom any correspondence should be addressed.

Contents

1. Introduction **2**
2. Experimental setup **3**
3. Calibration and reconstruction procedures **5**
4. Results **7**
4.1. Particle trajectories 7
4.2. Measurement of the forces 9
4.3. Radial and orthogonal contributions 13
4.4. Velocity distributions of the particles 14
4.5. Measurement of the friction coefficient 16
5. Summary **17**
Acknowledgments **18**
References **18**

1. Introduction

Dusty plasmas have attracted much attention in recent decades. For dusty plasmas containing micrometer-sized particles, the observation of evolving dust structures is possible by means of video imaging techniques. After the discovery of dust crystals in the 1990s [1]–[3], which were easily observed with a video microscope, research has now been extended to three-dimensional (3D) dust systems. Such 3D systems are found, for example, as Yukawa balls [4], in the secondary plasma above a biased pixel of a segmented electrode [5], and in dusty plasma environments under microgravity conditions [6, 7] where the apparent gravitation is reduced to a fraction of the earth's acceleration, $g = 9.81\,\mathrm{m\,s^{-2}}$. Under these microgravity conditions, it is possible to investigate extended 3D dust structures.

One way to achieve weightlessness is a parabolic flight, where the experiment is conducted in an aircraft that is following a parabolic flight path. Along this path, the weight can be compensated for a time of 22 s during a free fall of the aircraft, reducing the apparent gravitation to typically less than $0.05g$ during this time. From available 3D diagnostic methods, e.g. the color-gradient method [5], digital in-line holography [8, 9] and stereoscopic camera systems [10, 11], only stereoscopy is relatively insensitive to vibrations, making it ideal for investigations of parabolic flights, where vibrations from the aircraft are unavoidable.

The typical structure of a dust cloud under microgravity is a prominent central particle-free void surrounded by the extended dust cloud (see figure 1). The dust cloud itself is usually not in a stable state, but shows dynamic phenomena such as self-excited waves or instabilities. A number of investigations have been performed on various aspects of this dust dynamic (see e.g. [12]–[14]). For the investigation presented here, however, discharge parameters were adjusted to suppress dust cloud dynamics as far as possible. The remaining low wave activity is considered irrelevant to our analysis, as the void boundary is unaffected by those waves, and the dust cloud itself is considered to have no effects on particles inside the void region.

The void is considered to be formed by an outward-directed ion drag force due to ambipolar ion flux, which is at some point compensated for by an inward-directed electric field force [15]. At this point, where both forces cancel out, the void boundary is formed. A number of experiments on forces in the void region were performed earlier [16]–[18]. However, only a

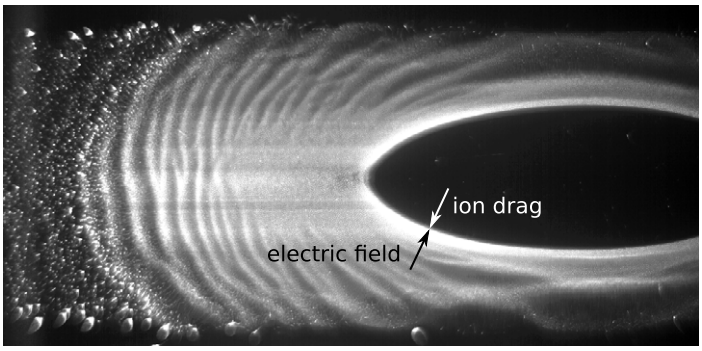

Figure 1. Two-dimensional (2D) slice of the dust structure under microgravity. The central, dust-free void is formed by an outward ion drag force and an inward electric field force, which balance each other at the void boundary.

thin slice of the void region could be observed in those experiments due to illumination by a laser sheet. Furthermore, the probe particles in these experiments were the same as in the surrounding dust cloud, which means that the probe particles are stopped at the void boundary, since they cannot penetrate this boundary due to the force equilibrium.

In our experiments, a mechanical dust accelerator is attached to the discharge chamber, which is used to inject fast particles into the discharge. These particles are chosen to be significantly larger than the particles forming the dust cloud, thus being able to penetrate the void boundary and, in principle, making the dust cloud itself available for force measurements. For the analysis of the 3D particle dynamics, a stereoscopic camera system was developed. With this setup, we were able to observe a large part of the void in 3D, giving us the possibility of investigating the full 3D dynamics of the dust particles inside the void region.

In this paper, first the stereoscopic system with three cameras, specifically designed for operation on parabolic flights, is described and a method for determination of 3D particle trajectories is explained. Using the trajectories of fast accelerator particles, the particle dynamics and force field inside the void are derived, analyzed and characterized in 3D.

2. Experimental setup

The experiments for this investigation were performed on a parabolic flight campaign in 2009, in close cooperation with the dusty plasma workgroup of the University of Kiel. Experiments are performed in a parallel-plate radiofrequency (rf) discharge in argon at gas pressures of typically $p = (10\text{–}50)\,\mathrm{Pa}$ and rf voltages of $U_{\mathrm{rf}} = (40\text{–}70)\,V_{\mathrm{pp}}$. Schematic sections through the discharge vessel are shown in figure 2; the discharge chamber is the same as that described earlier [19, 20], but with a simplified electrode setup. The dust cloud is formed by injecting small melamine-formaldehyde (MF) particles of $(6.84 \pm 0.07)\,\mu\mathrm{m}$ diameter into the plasma. There, the dust forms an axially symmetric cloud around the central, dust-free void. The discharge conditions are chosen to create a stable dust cloud with as low wave activity as possible. This was achieved for a gas pressure of $p = 15\,\mathrm{Pa}$ and an rf voltage of $U_{\mathrm{rf}} = 63\,\mathrm{V_{pp}}$.

For the injection of fast particles, a mechanical dust accelerator is mounted on one side of the chamber (see figure 2). This device generates a fast particle beam by means of a spinning cogwheel and a pinhole between the accelerator and the plasma chamber [21]. With this

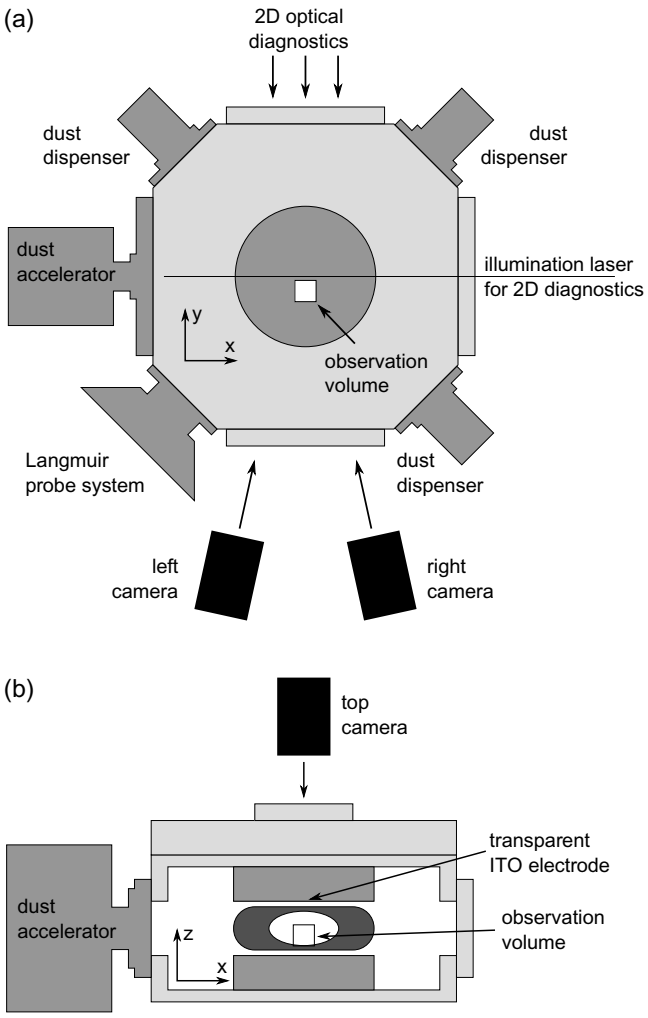

Figure 2. Schematic diagrams of the discharge chamber IMPF-K2 for parabolic flights. (a) Top view and (b) front view from the position of the stereoscopic side cameras. The observation volume of the stereoscopic camera setup can be moved along the y- and z-axis in this coordinate system.

setup, maximum theoretical particle velocities of up to $10\,\mathrm{m\,s^{-1}}$ are possible, while measured velocities range up to $(1\text{–}2)\,\mathrm{ms^{-1}}$ for the fastest detected particles [21]. The accelerator is equipped with polymethyl methacrylate (PMMA) particles of $(20.02 \pm 0.28)\,\mu\mathrm{m}$ diameter, which are decisively larger than those particles forming the dust cloud.

The stereoscopic camera setup, consisting of three synchronized high-speed CCD cameras with VGA resolution (640×480 pixels (px)) and a usable frame rate of up to 180 fps, is mounted on ball rails and can be moved vertically and horizontally by means of stepper motors. Therefore it is possible to position the observation volume (almost) freely inside the discharge volume. In the setup as it was used on the parabolic flights, the observation volume has a maximum extension of $(16 \times 15 \times 16)\,\mathrm{mm^3}$, but is, due to the camera arrangement, irregularly shaped and thus effectively somewhat smaller. Each camera reaches a spatial resolution of about $20\,\mu\mathrm{m\,px^{-1}}$. A schematic view of the complete camera setup and the mounting frame is shown in figure 3. The particles inside the observation volume are illuminated

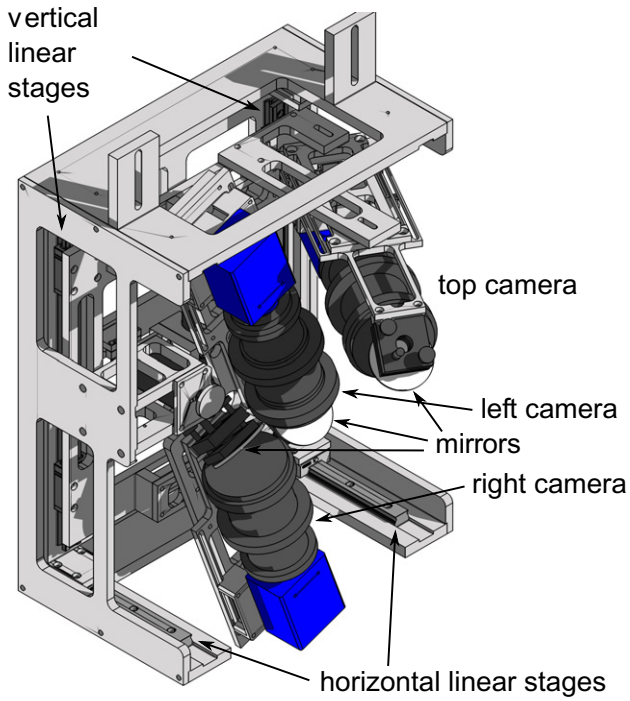

Figure 3. The stereoscopic camera setup used on parabolic flights. The cameras are mounted on a horizontally and vertically movable frame, which is driven by two stepper motors.

with a frequency-doubled 2.5 W Nd:YVO_4 laser at 457 nm wavelength, with the beam expanded to a diameter of 12 mm.

Due to restricted space in the experimental setup, all cameras view via adjustable mirrors into the discharge chamber. The mirrors of the two side cameras (and thus the cameras' optical axes) lie in a plane parallel to the electrode surfaces, the third camera is mounted above the top window of the chamber, with its optical axis nearly perpendicular to the electrodes. The top camera is of special importance in this setup, as the two side cameras alone, with a relatively narrow angle of approximately 25° between their optical axes, provide only poor spatial resolution along the *y*-direction. Due to its orthogonal line of sight (with respect to the two side cameras), the top camera can be used to overcome this problem, thus ideally giving similar spatial resolution in all three dimensions.

This stereoscopy system is designed to give the possibility of equipping the cameras with various lenses and has to be disassembled into several parts during integration into the experimental environment. Furthermore, movable parts like the mirrors might be affected by vibrations of the aircraft and lose their justified position during a flight. All of this makes it necessary to calibrate the system before each set of measurements, i.e. once before each flight day during a parabolic flight campaign.

3. Calibration and reconstruction procedures

Here, a brief summary of the camera calibration and particle reconstruction procedures is given. The complete calibration and reconstruction algorithm has been described in detail by Himpel *et al* [22].

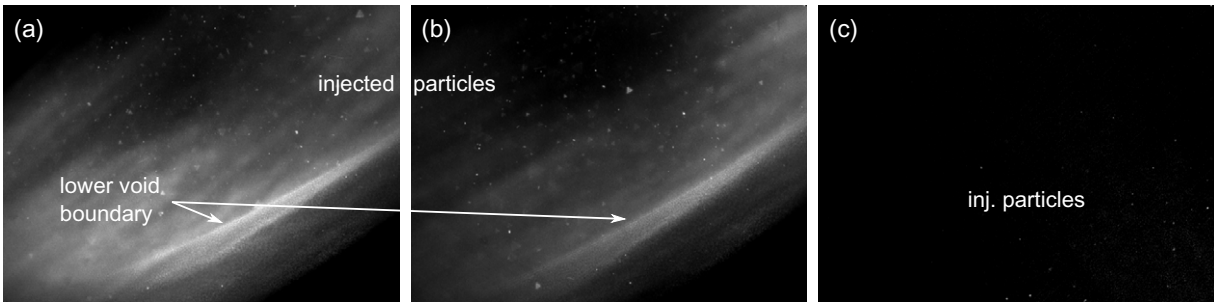

Figure 4. Raw camera images of accelerator particles inside the void in (a) the left camera, (b) the right camera and (c) the top camera. In these images, a set of approximately 100 particles is detected, resulting in more than 150 triangulated 3D particle positions.

The calibration of the camera system takes place via the simultaneous capture of a calibration grid pattern, which is mounted in the center of the discharge chamber. The grid can be rotated in two axes and thus allows one to cover a great part of the observation volume with calibration points. With a sufficiently large number of corresponding target points, the extrinsic (position, rotation) and intrinsic (focal length, skew, optical axis) camera parameters can be found by minimizing the projection error of a reconstructed 3D calibration point structure in each camera. In our case, a projection error of less than 0.5 px (approximately 10 μm) is achieved for the presented camera system.

The reconstruction procedure, which is used to build the full 3D particle trajectories from the camera images, is split into four tasks; (i) image processing and determination of the 2D particle coordinates in each camera, (ii) tracking of the 2D particle projections, (iii) 3D particle position reconstruction, and finally (iv) particle linking and tracking in order to create 3D trajectories.

In a first step, the raw camera images (as shown in figure 4) are cleaned by subtracting background light and static structures, such as the comparatively slow moving large dust cloud, by computing a local average image from images $f-10$ to $f+10$, where f is the current image number. In the subtracted image, only the fast particles and small-scale noise of the original image are retained. The 2D particle positions in the camera images are then detected using the algorithm of Crocker and Grier [23], which has been shown to be suitable for dusty plasma application [24] and allows one to measure the particle positions to sub-pixel accuracy.

In the so obtained datasets, the particles are tracked in each camera independently in 2D, i.e. for each projection in frame f, a projection in frame $f+1$ is searched that is produced by the same particle. This is done using an algorithm proposed by Ouellette *et al* [25], which uses a projection of a particle trajectory into the next frames to determine a possible successor particle. Of these 2D trajectories, only those are kept that have a length of at least three frames and thus are likely to be formed by real particles and not by artifacts in the images. Using these 2D particle trajectories, a triangulation of 3D particle positions is performed. With known 2D particle coordinates and the camera properties known from calibration, a ray can be constructed for each camera, along which the 3D particle has to be positioned. If camera calibration and 2D particle position measurement were possible without errors, the rays from all three cameras would intersect in a single point in 3D space, yielding one distinct particle

position. For the real experimental setup, however, such an intersection point will generally not exist, and a different approach has to be made. In our case, a geometric error cost function is used to minimize the projection error of the triangulated 3D point back into the cameras. This approach has been shown to be an optimum solution for the triangulation problem in terms of the triangulation error [26]. For such a triangulation, only corresponding particle projections, i.e. projections into the different cameras produced by the same particle, may be considered. These particle correspondences are determined using the epipolar geometry [27] of the camera system. For each particle in one camera, the epipolar lines in the remaining cameras are computed, and all particle projections within a small region around the epipolar line are considered as possible correspondences. For all possible triples of projections, a 3D particle position is triangulated, leading to a growing number of false 3D particle positions with higher particle densities. In the last step of reconstruction, all triangulated 3D particle positions are tracked through the frames in order to create the full particle trajectories. Here, particles resulting from false correspondences are effectively sorted out, since they can generally not be tracked over a large number of frames, and only those particle trajectories with a length of at least three frames are kept for further evaluation.

4. Results

4.1. Particle trajectories

Now, we analyze the trajectories of particles injected by the dust accelerator into the void. From the dataset of one parabola with approximately 8 s of fast particles moving through the void region, a total of 696 particle trajectories have been reconstructed. In order to extract the forces exerted on the particles by the plasma, the total force $\vec{F} = m_\mathrm{d}\ddot{\vec{r}}$ acting on the particles is computed. To reduce high-frequency noise, the original data are smoothed by a Savitzky–Golay filter [28], using a second degree polynomial with a window width of nine frames. From the smoothed data, the first derivative is computed to obtain the particle velocities; this is then again smoothed and used for computing the second derivative, namely the particle acceleration. For this procedure, only trajectories with a length of at least the filter's window width can be used, leaving a total of about 520 particle trajectories for evaluation. A sample trajectory is shown in figure 5, along with its derivatives. The open symbols represent the raw data in (a), the first derivative of the smoothed data in (b) and the derivative of the smoothed first derivative in (c). Solid lines are the Savitzky–Golay filtered data in all plots.

The particle's velocity data in all three axes show a decrease in the magnitude of velocity in time due to friction with the neutral gas (and the outward-directed forces inside the void region). Furthermore, especially in the particle's acceleration data (figure 5(c)), obvious oscillatory behavior at a frequency of approximately 20 Hz is seen, which is attributed to vibrations produced by the aircraft. Aircraft acceleration measurements taken during the flight show a distinct peak in the Fourier spectrum at 160 Hz, which corresponds to a frequency of 20 Hz when sampled at the camera frame rate of 180 Hz. The timescale on which the dust particles are able to follow changes in the surrounding plasma properties is given by the dust plasma frequency, $\omega_\mathrm{pd} = \sqrt{Z_\mathrm{d}^2 n_\mathrm{d} e^2/(\epsilon_0 m_\mathrm{d})}$. For an approximate dust charge of $Z_\mathrm{d} \approx 30\,000$ elementary charges and a dust density of $n_\mathrm{d} \approx 10^{10}\,\mathrm{m}^{-3}$, the dust plasma frequency for the dust particles observed here can be estimated as $\omega_\mathrm{pd} \approx 70\,\mathrm{s}^{-1}$ and $\omega_\mathrm{pd}/(2\pi) \approx 11$ Hz. Therefore, the dust clearly cannot follow the measured frequency of 160 Hz, and thus the observed oscillations are likely due to

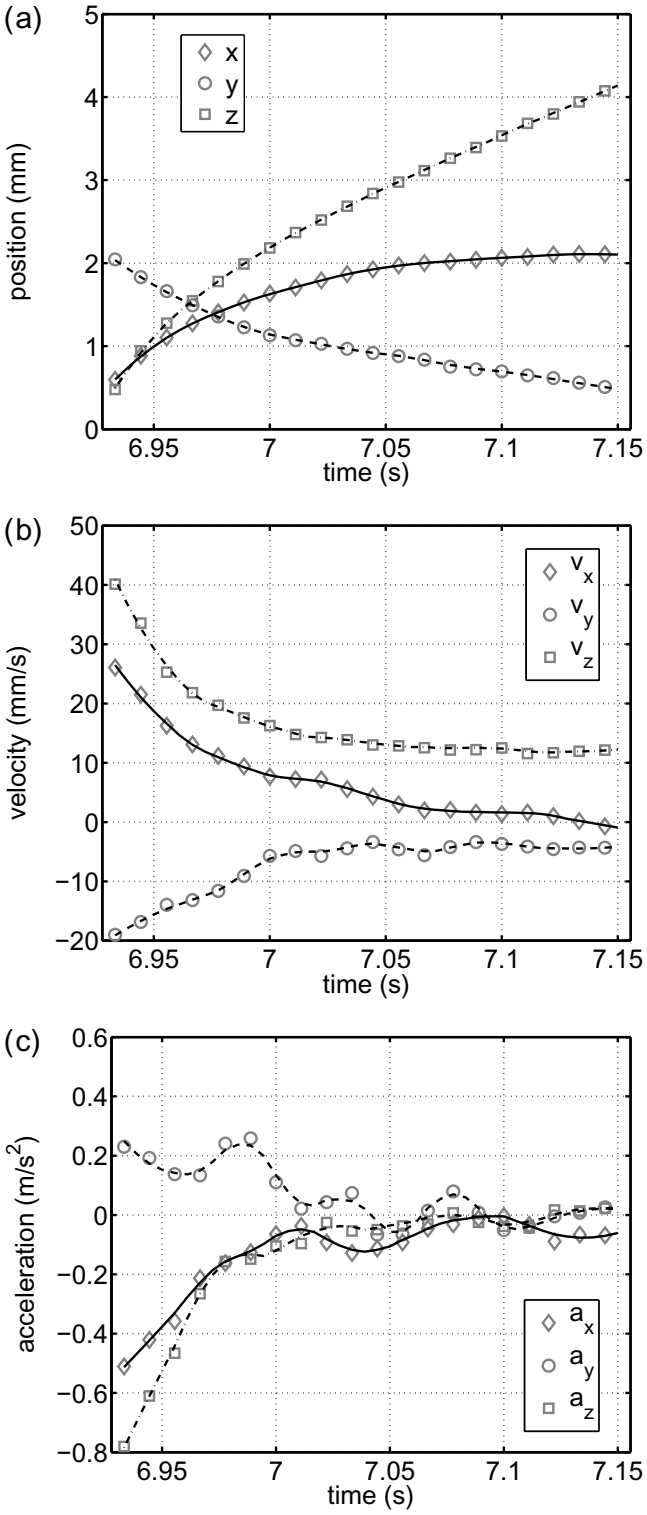

Figure 5. Trajectory of a selected particle with a length of 40 frames. The graphs show the three components, namely (a) the particle position, (b) the particle velocity and (c) the acceleration. The graphs show the three components of (a) the raw data, (b) the first derivative of smoothed raw data and (c) the derivative of the smoothed first derivative. Solid lines are Savitzky–Golay filtered data.

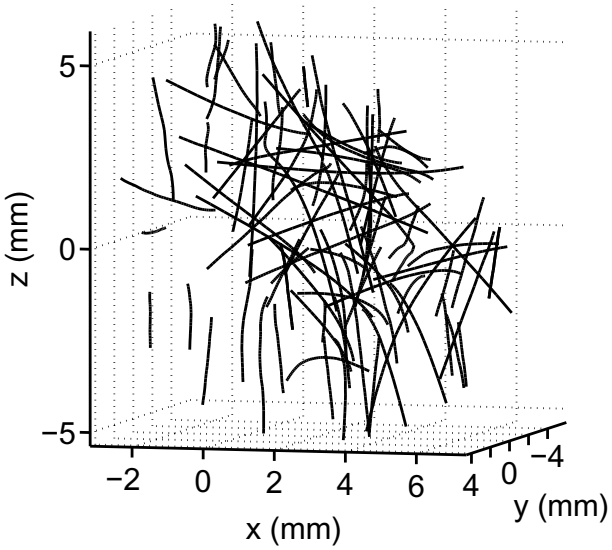

Figure 6. Reconstructed 3D particle trajectories with a length of at least 20 frames. The data are given in the chamber's coordinate system, i.e. the xy-plane is parallel to the electrodes' surfaces and z-points from the lower to the upper electrode.

mechanical vibrations of the camera mounting frame. This assumption is supported by the fact that the oscillations are visible in all trajectories, with the same frequency and the same phase for all particles at a given time. Therefore, any seemingly oscillatory movement of the particles is obviously added by external processes and is not to be interpreted as real particle movement.

4.2. Measurement of the forces

The trajectories used for the force computation are shown in figure 6. For clarity, only trajectories with a length of at least 20 frames are shown. The data are given in the chamber's coordinate system, i.e. the xy-plane is parallel to the electrodes' surface and the z-axis points upwards with the origin in the chamber center. From the complete dataset, the force acting on each particle at every point of its trajectory is determined. The total force on a particle is given by

$$\vec{F}_{\mathrm{tot}} = m_{\mathrm{d}}\ddot{\vec{r}} = \vec{F}_{\mathrm{frict}} + \vec{F}_{\mathrm{el}} + \vec{F}_{\mathrm{ion}} + \vec{F}_{\mathrm{z}}, \tag{1}$$

with the friction (or neutral drag) force F_{frict}, the electric field force F_{el}, the ion drag force F_{ion} and the force resulting from the residual z-acceleration F_{z}; additional forces, such as thermophoresis or particle–particle interactions, are omitted here, since there is no temperature gradient present and the density of accelerated particles is low enough to ensure negligible particle–particle electrostatic repulsion. The forces considered here are applicable independent of the discharge parameters and cover the complete range of forces that might arise for a dust particle immersed in a plasma. For an overview and discussion of forces acting on dust particles in complex plasmas, see e.g. [29].

The z-acceleration is kept below $|a_z| = 0.02g$ during this parabola (see figure 7), resulting in a force on the particles of $|F_z| < 9.8 \times 10^{-13}$ N for the PMMA particles

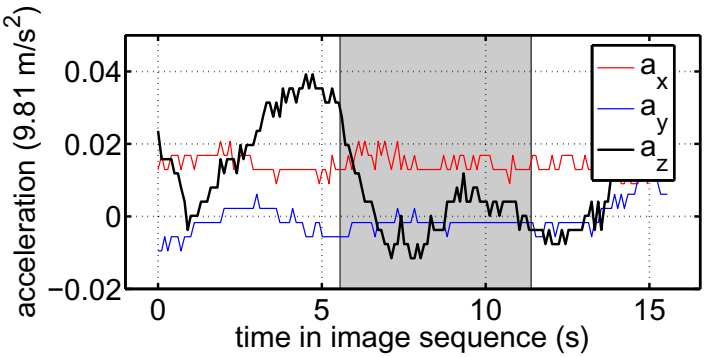

Figure 7. Residual gravity a_z and accelerations in the x- and y-direction (a_x, a_z) for the time of the image sequence being evaluated. The gray area marks the part of the sequence in which particles are reconstructed. For most of this time, residual gravity is well below $0.02g$.

($m_d = 4.99 \times 10^{-12}$ kg). The neutral drag force is given by $\vec{F}_{\text{frict}} = -m_d \beta \dot{\vec{r}}$, with the Epstein friction coefficient,

$$\beta = \delta \frac{8}{\pi} \frac{p}{a \rho_d v_{\text{th,n}}}. \tag{2}$$

Here, δ is a coefficient describing how neutral gas atoms are reflected from the particle's surface with $\delta = (1.0 \ldots 1.442)$ [30], p the gas pressure, a the particle radius and $v_{\text{th,n}}$ the mean thermal velocity of the neutral gas atoms. The coefficient δ has been experimentally determined [31] to be $\delta = 1.26 \pm 0.13$ for MF microspheres in dusty plasmas. This value will be used in our calculations. With a gas pressure of $p = 15$ Pa, a particle radius of $a = 10.01\ \mu$m and the PMMA mass density of $\rho_d = 1190\,\text{kg}\,\text{m}^{-3}$, the friction coefficient is calculated as $\beta = (10 \pm 1)\,\text{s}^{-1}$. With this coefficient, the neutral gas drag can be calculated from the particle's velocity at each time of the trajectory, and the sum of the electric field force and the ion drag force can be obtained.

With a particle velocity $|\dot{\vec{r}}| \geqslant 1\,\text{cm}\,\text{s}^{-1}$ throughout the trajectory (see figure 5(b)), the friction force is calculated as $F_{\text{frict}} \geqslant 5.1 \times 10^{-13}$ N, and will be significantly larger than this value for the greater part of the trajectory. This value is of the same order of magnitude as the force resulting from residual z-acceleration. In order to exclude the effects of the z-acceleration, we have evaluated the movement of the void along the z-axis with respect to the chamber center during the time of the image sequence. From this measurement, we obtained the time-resolved position of the void center, $z_{\text{void}}(t)$, which is then used to correct all particle positions using $z_{\text{corr}}(t) = z_{\text{meas}}(t) - z_{\text{void}}(t)$. The corrected z-coordinates of the particles then do not contain any global fluctuations from residual z-acceleration, and thus the influence of the z-acceleration can be neglected in further evaluations.

The remaining forces, F_{el} and F_{ion}, cannot be separated without detailed knowledge of the surrounding plasma (e.g. potential distribution and ion flow velocity) and will hereafter be referred to as plasma forces F_{pl}, with $F_{\text{pl}} = F_{\text{el}} + F_{\text{ion}}$. This force is extracted for all particles at each available time step of the trajectory. The full set of 3D particle trajectories is shown in figure 8 with the force magnitude color-coded along the path of the trajectory. For clarity, projections of the 3D force field onto the xy- (top view), xz- (front view) and yz-plane (side view) are shown along with the position of the surrounding dust cloud.

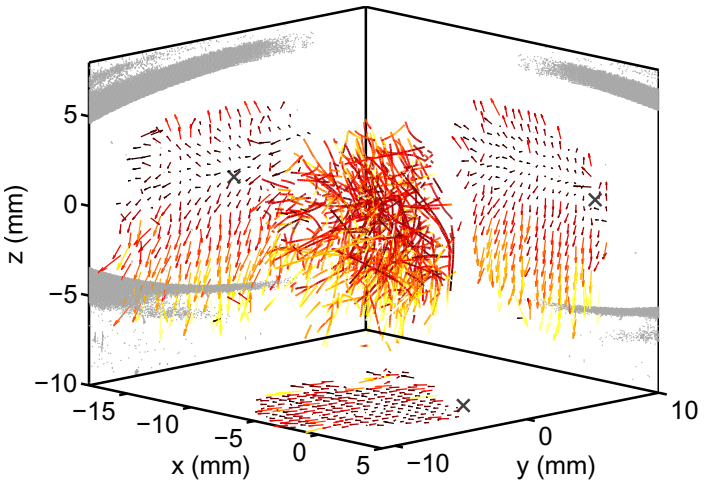

Figure 8. The full set of 3D particle trajectories. The force value is color-coded, with the smallest force values being the darkest colors. The 2D projections of the force field onto the xy-, xz- and yz-plane are shown along with the estimated position of the void center (marked by $\times$), which is defined by the region of the lowest force values.

To further illustrate the nature of the force field, the 3D data are transformed into cylindrical coordinates, using the void center as the origin for the coordinate system. This is a reasonable transformation, since the discharge chamber and thus the void are axially symmetric around the z-axis. The position of the void center ideally coincides with the origin of the chamber's coordinate system, but in reality deviates from this position due to residual acceleration in all directions and disturbances inferred from the dust accelerator. Therefore, the void center is estimated from the projections of the force field onto the xy-, xz- and yz-plane, using the region with the smallest force values as void center position estimate. This estimate is marked in the force field projections in figure 8. Furthermore, the void center can be obtained by evaluating additional optical 2D diagnostics, where a slice through the center of the discharge is observed (see figure 2). From these observations, the void position and extension can be calculated relative to the chamber center, and from the calibration target data of the stereoscopic camera systems it can be transferred into the stereo coordinate system. The 3D force field in the 2D cylindrical projection is then averaged in a grid of 20×20 fields, averaging over typically more than 30 single values in each field. The resulting force field is shown in figure 9. Here, the direction of the force (figure 9(a)) is shown together with its magnitude (figure 9(b)). It is clearly seen that the force field is generally directed outwards and is increasing in its value toward the void boundary. Due to plasma disturbances caused by the dust accelerator, the void's shape is not constant over the time of one parabola. This void shape change is reflected in the thickness of the illustrated void boundary region, which is a 1σ-environment around the mean void boundary position for each radial distance from the void center.

From figure 9(a), a change in direction of the force can be observed for the dust passing the lower void boundary. It has again to be pointed out that due to their larger size, the accelerator particles (20.02 μm PMMA) used for the force field measurement do not reach an equilibrium position at the void edge, which is defined by the equilibrium position of the smaller, dust-cloud-forming particles (6.84 μm MF). The combination of a higher electric field force and an

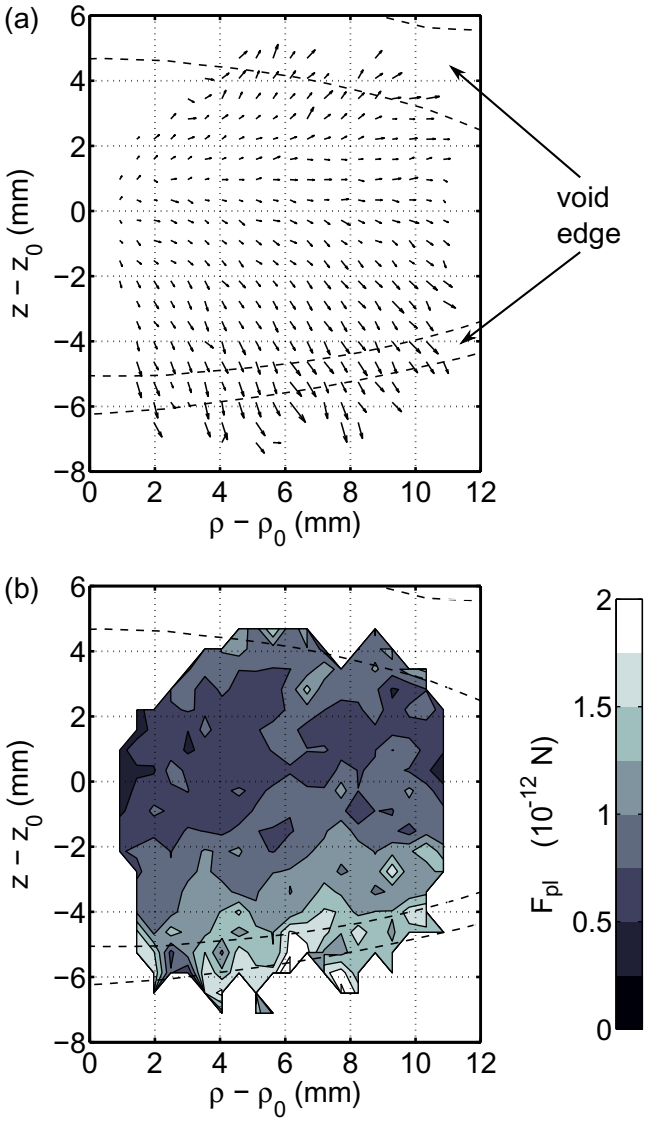

Figure 9. Plasma forces F_{pl} in the void region. (a) Direction of the force; (b) magnitude of the force in 10^{-12} N. Both the outward-pointing direction and the increasing force values at larger distances from the void center are in good agreement with the expectations.

increased ion drag for the larger particles results in an equilibrium position for the accelerator particles, which lies beyond the void boundary formed by the smaller dust cloud particles. Due to the higher particle density in the dust cloud and the difficulties in tracking the particle trajectories in high dust density regions, this equilibrium position cannot be observed in the present measurements.

The magnitude of the plasma forces acting on the particles inside the void region, shown in figure 9(b), ranges from $F_{\mathrm{pl}} < 0.5 \times 10^{-12}$ N in the central void region to $F_{\mathrm{pl}} > 1.5 \times 10^{-12}$ N at the void edge. From Langmuir probe measurements in the same chamber at comparable discharge conditions [32] (there, $p = 20$ Pa and $U_{\mathrm{rf}} = 40$ (60) V at the ring (disc)

electrode), the plasma parameters at $\rho \approx 5\,\mathrm{mm}$, $z = 0\,\mathrm{mm}$ can be estimated as $T_e \approx 3.5\,\mathrm{eV}$, $n_e = n_i \approx 5 \times 10^{14}\,\mathrm{m}^{-3}$ and $E \approx 400\,\mathrm{V\,m}^{-1}$. From these values, the dust charge is calculated as $q_d \approx -28500e$ using the collision-corrected charging model of Khrapak *et al* [33]. This value for the dust charge is supported by calculations performed by Ikkurthi *et al* [34], where a dust potential of $\approx -4\,\mathrm{V}$ (resulting in a dust charge $q_d = -27800e$ using the spherical capacitor model) is calculated in the plasma bulk for a particle of $10\,\mu\mathrm{m}$ radius. Using these values of plasma parameters and dust charge and an ion flow velocity $v_i = \mu E \approx 375\,\mathrm{m\,s}^{-1}$ [35], the (collisionless) ion drag model of Hutchinson [36] yields an outward-directed ion drag force of $F_{ion} \approx 2.4 \times 10^{-12}\,\mathrm{N}$, which is opposed by an inward-directed electric field force of $F_{el} \approx 1.8 \times 10^{-12}\,\mathrm{N}$. From numerical computations of the ion drag in collisional plasmas [37], with a collisionality parameter $\nu/(T_e/m_i)^{1/2}/a = 5 \times 10^{-3}$ for our situation, ion-neutral collisions would increase the ion drag force by roughly 25%, yielding a maximum collisional ion drag force of $F_{ion} \approx 3 \times 10^{-12}\,\mathrm{N}$. This results in a total outward force of $F_{pl} = F_{ion} - F_{el} \approx (0.6\text{–}1.2) \times 10^{-12}\,\mathrm{N}$, which is in good agreement with the values obtained from our measurements (see figure 9(b)). The ion flow velocity v_i used in our analysis is of the order of the ion thermal velocity, which is in good qualitative agreement with theoretical results of Goree *et al* [15] and Tsytovich *et al* [38] for suitable parameters.

Assuming for further comparison that the force decreases linearly from the void edge to the void center, i.e. $F_{pl} = kr$ with $r = \sqrt{(z - z_0)^2 + (\rho - \rho_0)^2}$, the force constant k can be estimated from a comparison of the forces at the void center and the void boundary. For our measurements, this results in a force constant $k = (1.4 \pm 0.4) \times 10^{-10}\,\mathrm{N\,m}^{-1}$. Wolter *et al* found a value of $k = (1.6 \pm 0.4) \times 10^{-11}\,\mathrm{N\,m}^{-1}$ close to the void boundary for particles of $6.84\,\mu\mathrm{m}$ diameter [18], while Kretschmer *et al* obtained two different values, $k_1 = (1.25 \pm 0.03) \times 10^{-11}\,\mathrm{N\,m}^{-1}$ and $k_2 = (0.27 \pm 0.01) \times 10^{-11}\,\mathrm{N\,m}^{-1}$, for different regions inside the void using particles with diameters of 1.7 and $3.4\,\mu\mathrm{m}$ [17]. The deviation of our value for k from the values obtained by the other two experiments is easily explained by the different particle sizes, as the total force increases for larger particles. Therefore, the particles used in our experiment (with a diameter of $20.02\,\mu\mathrm{m}$) will experience the strongest force, thus being in good agreement with earlier experiments.

4.3. Radial and orthogonal contributions

The force field inside the void region is generally considered to be radial in shape, which can be considered true in the xy-plane. In the z-direction, the orientation of the force will deviate from the strictly radial shape at larger distances from the void center due to the oblate form of the void. With our stereoscopic camera system, we are for the first time able to resolve the full 3D properties of the force field inside the void region. Therefore, we now have the possibility of testing the assumption of a radial shape of the force field. First, we decompose the forces at each available position in the void into a radial part $\vec{F}_{rad} = (\vec{F}_{pl} \cdot \vec{r})/r^2\,\vec{r}$ and an orthogonal part $\vec{F}_{orth} = \vec{F}_{pl} - \vec{F}_{rad}$. The radial and orthogonal parts are again projected onto the ρ–z-plane and averaged as described above. The results are shown in figure 10. Comparing the decomposition of the force in figure 10 with the profile of the total force in figure 9(b), the overall shape of the force field is generally dominated by radial forces in the central region of the void. The orthogonal part of the force grows in influence with larger radial distances from the void center, which is easily explained by the oblate form of the void, which necessarily leads to deviations of the force direction from a strictly radial form. The relatively high values of the measured

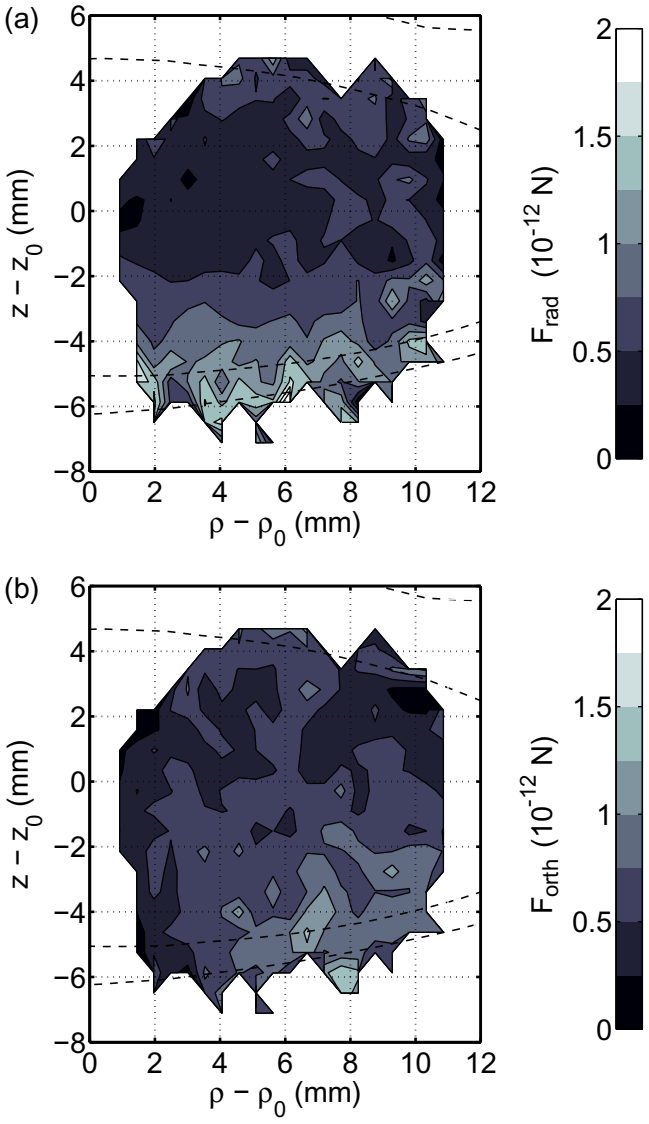

Figure 10. Decomposition of the plasma forces in the void region into (a) the radial part and (b) the orthogonal part. Clearly, the overall shape of the total force field (figure 9(b)) is mainly determined by the forces pointing radially outwards from the center of the void. The orthogonal part is almost constant throughout the observation volume.

orthogonal forces may additionally be due to the vibrations and the corresponding oscillations in the particle trajectories shown in figure 5(c). Considering these effects, it seems justified to conclude that in a large part of the observation volume, close to the void center, the force field is pointing in fact radially outwards.

4.4. Velocity distributions of the particles

This radial character of the field should also reflect in the velocity distribution functions of the particles. For all particles entering the discharge, the velocity distribution is determined by the

properties of the dust accelerator. Most of the particles, however, are detected after a reflection from the wall opposite to the accelerator, and thus the velocity distribution will be randomized by reflections from the walls of the chamber. A second source for a random velocity distribution is that the fast accelerator particles may perform collisions with the smaller, dust-cloud-forming particles. Hence, decomposing the velocity at the detection of the accelerator particles again into a radial and an orthogonal part, one would expect a broad non-radial distribution and only small radial contributions. On leaving the void, the particles' velocity should be influenced by the force field, which should express in a significantly narrower non-radial distribution peaking at lower absolute values of the orthogonal part of the velocity, while the radial part should be considerably shifted to higher velocities.

To measure the influence of the force field on the particle velocities, we have collected the velocity distributions at the first and the last point of each trajectory. The first detection of a particle, and thus the first point of a trajectory, is assumed to be the instant when the particle enters the void, while at the last point of the trajectory the particle has moved through the void for some time and leaves it on a path that is predominantly governed by the character of the force field. The resulting velocity distributions are shown in figure 11, where the first column of graphs shows the velocity distributions at the first trajectory points, whereas the second column shows the situation at the last frames. Obviously, all distributions at the end of the trajectories are narrower than the corresponding distributions at the detection time, showing that fast particles are significantly affected by friction and particles lose their velocity on their path through the void. The radial velocity component (figures 11(a) and (d)) is shifted to slightly higher velocities at the end of the trajectories, which is caused by the conversion of the initially undirected movement of the particles into one with the radial character of the force field.

The effect on the orthogonal part of the particle velocities (figures 11(b) and (e)) is less pronounced, but follows the expectations: while the distribution at the injection time is relatively broad with many high-velocity contributions, it is compressed at lower particle velocities at the end of the trajectories. Comparing radial and orthogonal parts at the injection time (figures 11(a) and (b)) and at the end of the trajectories (figures 11(d) and (e)), the particles' movement is significantly influenced by orthogonal contributions at the injection time, and shows an obvious transformation into a more radial velocity profile at the end of the trajectories. This again supports our conclusion that, despite the high orthogonal forces from figure 10(b), the force field is in fact radial and pushes the particles on radial paths out of the void.

The distributions of the total particle velocity, again at the injection time and at the end of the trajectories (figures 11(c) and (f)), show results that are consistent with radial and orthogonal decomposition. At the injection time, the distribution is again relatively broad with many high-velocity parts, and shrinks to the end of the trajectories to a narrow distribution with a pronounced peak at the most probable velocity $v_p \approx 11\,\mathrm{mm\,s^{-1}}$. This value can serve directly as a check for consistency of the velocities with the forces that have been measured before. Assuming an equilibrium of plasma forces and friction at the end of the trajectories, i.e. $\vec{F}_{pl} = -m_d \beta \dot{\vec{r}}$, a force value can be computed from the most frequent velocity that should coincide with the measured values of the force in figure 9(b). With the dust used here, the gas friction coefficient $\beta = (10 \pm 1)\,\mathrm{s^{-1}}$ and the most probable velocity v_p, a force of $F_{pl} = 0.56 \times 10^{-12}\,\mathrm{N}$ is obtained. This value is in good agreement with the values we measured for the force inside the void, which are $F_{pl} = (0.5\text{–}1.5) \times 10^{-12}\,\mathrm{N}$.

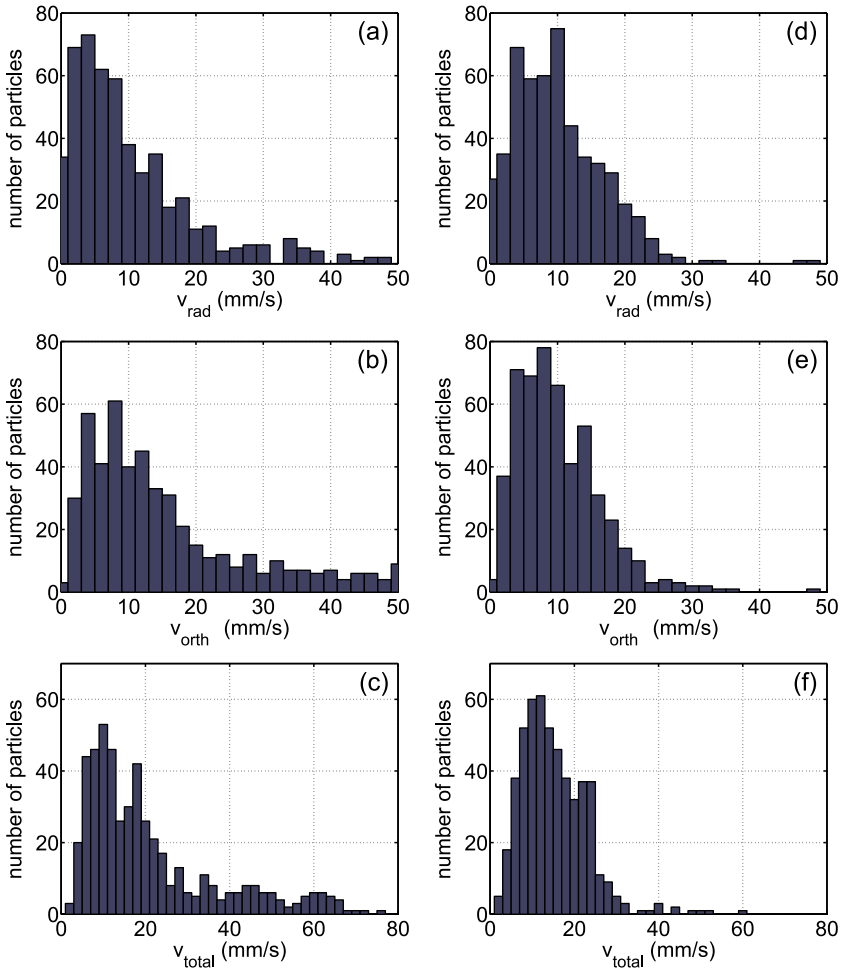

Figure 11. Decomposition of particle velocity distributions at injection time (a–c) and on leaving the void (d–f) into radial (a, d) and orthogonal (b, e) parts and total velocity values (c, f).

4.5. Measurement of the friction coefficient

On the other hand, under the assumption of a strictly radial force field and excluding any external disturbances, the structure of the force field can be used to measure the friction coefficient β for the particles. In a strictly radial field with no external vibrations, the plasma force acting on each particle at each time step along its trajectory has to point exactly radially outwards. This is mainly true for the forces in the xy-plane, since the oblate form of the void causes significant deviations from the radial field in the z-direction. In such a strictly radial force field, the condition for the plasma forces is $\vec{F}_{\mathrm{pl,xy}} \parallel \vec{r}_{xy}$, where $\vec{r}_{xy}$ is the position vector of a measurement. Following this condition, one can try to adjust the friction force, $\vec{F}_{\mathrm{frict}} = -m_{\mathrm{d}}\beta\dot{\vec{r}}$, in order to obtain a plasma force contribution $\vec{F}_{\mathrm{pl}} = \vec{F}_{\mathrm{tot}} - \vec{F}_{\mathrm{frict}}$ that fulfills the above condition. Here, we vary the friction coefficient β until we obtain a strictly radial plasma force, yielding an estimate for the friction coefficient β. The result of this analysis with our data is shown in figure 12. The relatively broad distribution peaks at $\beta \approx 10\,\mathrm{s}^{-1}$, which corresponds well with the theoretical value of $\beta = (10 \pm 1)\,\mathrm{s}^{-1}$ (dashed line). However, there are a significant number

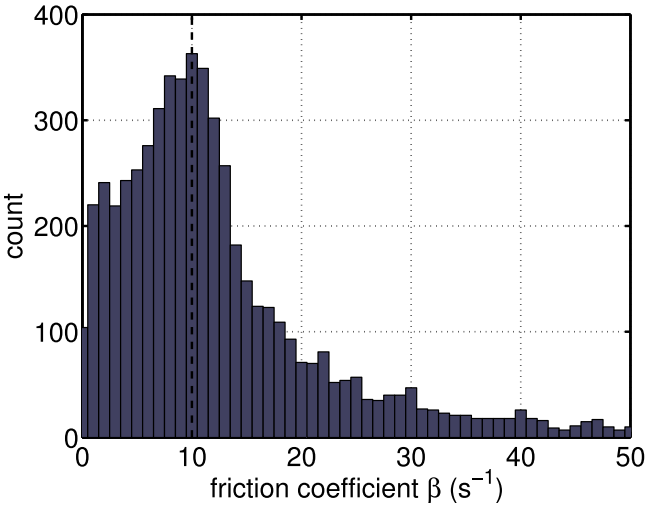

Figure 12. Values of β extracted from the assumption of strictly radial (in the xy-plane) forces on the trajectory. The peak around $\beta = 10\,\mathrm{s}^{-1}$ corresponds well to the theoretical value of $\beta = (10 \pm 1)\,\mathrm{s}^{-1}$ (dashed line).

of lower values of β. From equation (2), the value of β is linked with the particle radius a, with lower values of β corresponding to larger particles. One might speculate that larger particles are formed by collisions of the accelerator particles with smaller particles inside the dust cloud. This effect of dust agglomeration has recently been studied by Du *et al* [39]. However, the assumptions made for the determination of β (i.e. a strictly radial force field profile in the xz-plane and the exclusion of any external disturbances) are most probably not fully satisfied and any deviation from these ideal conditions will also lead to a broadening of the distribution of the measured values of β.

5. Summary

A stereoscopic camera setup of three cameras for use on parabolic flight experiments is presented. This setup allows the reconstruction of 3D movement of individual particles where the dust density in the plasma is not too high. For this setup, calibration and reconstruction procedures were developed and presented. With our reconstruction algorithm, we were able to reconstruct and individually track several hundreds of particles injected into the void region of a dusty plasma under microgravity conditions. From the particle trajectories, we have derived the forces acting on the particles inside the void. The so measured force values very well match estimations obtained using the ion drag models of Hutchinson and Patacchini and a dust charging model of Khrapak. Under the assumption of a linear dependence of the force on the distance to the void boundary, our measurements show overall good agreement with earlier experiments, considering the different discharge conditions and dust particle sizes.

We were, furthermore, able to resolve the full 3D structure of the force field in terms of radial and orthogonal contributions. This investigation has shown that the force field is in fact dominated by the contributions pointing radially outwards in x and y, while deviations from this radiality in the z-direction are unavoidable due to the oblate form of the void caused by the geometry of the discharge volume. We have measured the influence of the force field on the

injected fast particles and found that the particles' velocity distributions significantly change from the beginning to the end of each particle's trajectory. Here, the radial character of the force field is clearly reflected in the form of the velocity distributions. In addition, we have used the radial shape of the force field to measure the friction coefficient β for the probe particles, showing very good agreement with the theoretical value.

With this investigation, we have shown that our stereoscopic diagnostic is an ideal tool for the analysis of 3D particle dynamics on a single particle level inside the void region of dusty plasmas under microgravity conditions.

Acknowledgments

Financial support from the German Aerospace Center DLR, contract nos 50WM0738 and 50WM1138, is gratefully acknowledged. We thank our colleagues A Piel, O Arp, D Caliebe and K Menzel at the University of Kiel for fruitful collaboration.

References

[1] Thomas H M, Morfill G E, Demmel V, Goree J, Feuerbacher B and Möhlmann D 1994 *Phys. Rev. Lett.* **73** 652
[2] Chu J H and I L 1994 *Phys. Rev. Lett.* **72** 4009
[3] Hayashi Y and Tachibana K 1994 *Japan. J. Appl. Phys.* **33** L804
[4] Arp O, Block D, Piel A and Melzer A 2004 *Phys. Rev. Lett.* **93** 165004
[5] Annaratone B M, Antonova T, Goldbeck D D, Thomas H M and Morfill G E 2004 *Plasma Phys. Control. Fusion* **46** B495
[6] Morfill G, Thomas H M, Konopka U, Rothermel H, Zuzic M, Ivlev A and Goree J 1999 *Phys. Rev. Lett.* **83** 1598
[7] Thomas H M, Goldbeck D D, Hagl T, Ivlev A V, Konopka U, Morfill G, Rothermel H, Sütterlin R and Zuzic M 2001 *Phys. Scr.* **T89** 16
[8] Kroll M, Harms S, Block D and Piel A 2008 *Phys. Plasmas* **15** 063703
[9] Kroll M, Schablinski J, Block D and Piel A 2010 *Phys. Plasmas* **17** 013702
[10] Käding S and Melzer A 2006 *Phys. Plasmas* **13** 090701
[11] Käding S, Block D, Melzer A, Piel A, Kählert H, Ludwig P and Bonitz M 2008 *Phys. Plasmas* **15** 073710
[12] Schwabe M, Rubin-Zuzic M, Zhdanov S K, Thomas M H and Morfill G E 2007 *Phys. Rev. Lett.* **99** 095002
[13] Menzel K O, Arp O and Piel A 2010 *Phys. Rev. Lett.* **104** 235002
[14] Zhdanov S K *et al* 2010 *New J. Phys.* **12** 043006
[15] Goree J, Morfill G E, Tsytovich V N and Vladimirov S V 1999 *Phys. Rev.* E **54** 7055
[16] Thomas E Jr, Annaratone B M, Morfill G E and Rothermel H 2002 *Phys. Rev.* E **66** 016405
[17] Kretschmer M, Khrapak S A, Zhdanov S K, Thomas H M, Morfill G E, Fortov V E, Lipaev A M, Molotkov V I, Ivanov A I and Turin M V 2005 *Phys. Rev.* E **71** 056401
[18] Wolter M and Melzer A 2007 *Phys. Plasmas* **14** 123707
[19] Piel A, Klindworth M, Arp O, Melzer A and Wolter M 2006 *Phys. Rev. Lett.* **97** 205009
[20] Piel A, Klindworth M, Arp O, Melzer A and Wolter M 2007 *Phys. Rev. Lett.* **99** 209903
[21] Caliebe D 2010 private communication
[22] Himpel M, Buttenschön B and Melzer A 2011 Three-view stereoscopy in dusty plasmas under microgravity: a calibration and reconstruction approach *Rev. Sci. Instrum.* submitted
[23] Crocker J C and Grier D G 1996 *J. Colloid Interface Sci.* **179** 298
[24] Ivanov Y and Melzer A 2007 *Rev. Sci. Instrum.* **78** 033506
[25] Ouellette N T, Xu H and Bodenschatz E 2006 *Exp. Fluids* **40** 301–13
[26] Hartley R I and Sturm P 1997 *Comput. Vis. Image Underst.* **68** 146

[27] Zhang Z 1998 *Int. J. Comput. Vis.* **27** 161
[28] Savitzky A and Golay M J E 1964 *Anal. Chem.* **36** 1627
[29] Piel A 2010 *Plasma Physics* (Berlin: Springer)
[30] Epstein P S 1924 *Phys. Rev.* **22** 710
[31] Liu B, Goree J, Nosenko V and Boufendi L 2003 *Phys. Plasmas* **10** 9
[32] Klindworth M, Arp O and Piel A 2007 *Rev. Sci. Instrum.* **78** 033502
[33] Khrapak S A *et al* 2005 *Phys. Rev.* E **72** 016406
[34] Ikkurthi V R, Katyash K, Melzer A and Schneider R 2008 *Phys. Plasmas* **15** 123704
[35] Frost L S 1957 *Phys. Rev.* **105** 357
[36] Hutchinson I H 2006 *Plasma Phys. Control. Fusion* **48** 185
[37] Patacchini L and Hutchinson I H 2008 *Phys. Rev. Lett.* **101** 025001
[38] Tsytovich V N, Vladimirov S V, Morfill G E and Goree J 2001 *Phys. Rev.* E **63** 056609
[39] Du C R, Thomas H, Ivlev A, Konopka U and Morfill G 2010 arXiv:1007.4911v1